Macromolecular Materials and Engineering

www.mame-journal.de

RESEARCH ARTICLE OPEN ACCESS

Processing Characteristics of High Molecular Weight Polyethylene in Laser Sintering: The Role of Carbon Black Concentration and Processing Strategy for Diode Laser Sintering Machines

Christopher Krüsener | Ulrich A. Handge

Department of Mechanical Engineering, Chair of Plastics Technology, TU Dortmund University, Dortmund, Germany

Correspondence: Ulrich A. Handge (ulrich.handge@tu-dortmund.de)

Received: 21 March 2025 | **Revised:** 6 June 2025

Funding: The authors received no specific funding for this work.

Keywords: carbon black | high molecular weight | laser sintering | polyethylene | powder bed fusion

ABSTRACT

Until now, most results on processing high molecular weight polyethylene (HMWPE) in laser sintering (PBF-LB/P) have been achieved using industrial machines with a CO_2 laser. The use of diode laser sintering machines could make new materials more accessible to a wider audience. In this study, the role of carbon black (CB) concentration and processing strategy in HMWPE processing using diode laser PBF-LB/P machines is investigated. This work reveals that the carbon black concentration strongly influences processing, as it affects both absorption and specific heat capacity. Changes of specific heat capacity impact thermal balance during processing. Due to its narrow sintering window, HMWPE exhibits a high tendency for curling, which can be mitigated by reducing the scanning area and layer thickness. A suitable CB concentration ranges from 0.25 to 0.5 wt.%. In general, mechanical properties improve with volume energy density. This effect is caused by a more pronounced particle coalescence and interlayer bonding. However, the absorption properties of carbon black have a stronger impact on the mechanical properties than the energy input for the tested parameters. Mechanical tests on fabricated tensile bars reveal brittle fracture, which results from the high melt viscosity of HMWPE and the resulting delayed coalescence of particles.

1 | Introduction

Polyethylene is a semi-crystalline commodity polymer that can be synthesized in a wide range of molecular weights. The average molecular weight ranges between 0.5×10^6 and 1.0×10^6 g mol^{-1} for HMWPE and above 10^6 g mol^{-1} for UHMWPE [1–3]. The higher average molecular weight of HMWPE and UHMWPE leads to longer polymer chains compared to conventional high-density polyethylene (HDPE) [4]. Those longer polymer chains lead to a higher number of entanglements and therefore to a significantly higher melt viscosity than for HDPE. The melt viscosity for UHMWPE ranges between 10^6 and 10^8 Pa s [5, 6]. This is one main reason why the processing technologies for HMWPE and UHWMPE are mainly compression molding and RAM extrusion [7, 8]. Processing with injection molding in a proper way is not possible yet, either. However, compression molding and RAM extrusion are limited in view of the geometrical complexity of manufactured parts [7, 8]. Another way to process UHMWPE was introduced by Smith and Lemstra in 1980 [9]. The authors used solution spinning for the production of UHMWPE filaments. Hereby, the authors dissolved 2 %w/w of UHMWPE in decalin and investigated the influence of the draw ratio on the mechanical

https://doi.org/10.1002/mame.202500128

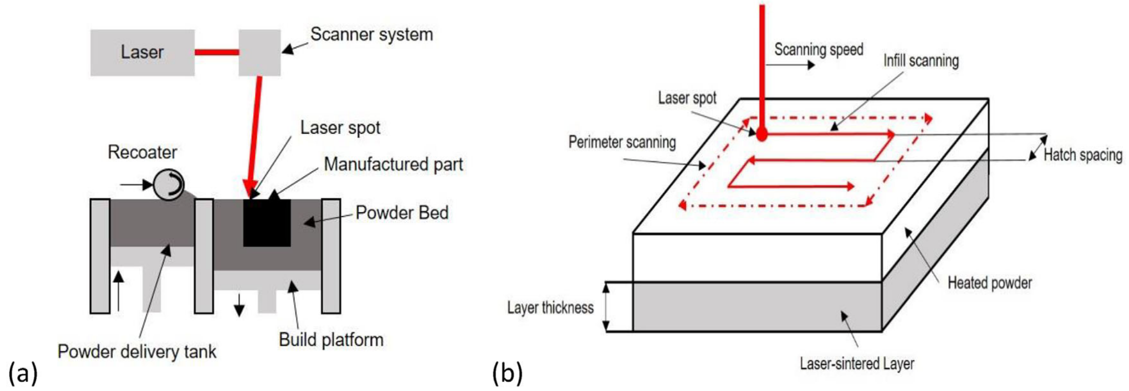

FIGURE 1 | Scheme of (a) an apparatus for the PBF-LB/P process and (b) movement of the laser spot.

and thermal properties of the fibers [9]. A similar processing method of UHMWPE was reported by Schaller et al. [10]

Additive Manufacturing (AM) includes all manufacturing processes that manufacture components by joining material together [11–14]. Hereby, the material can be a polymer, metal, ceramic or composite. One of the main advantages of AM is that there is nearly no limit in view of the geometrical complexity of manufactured parts [11, 12, 15]. This makes AM very attractive for all applications where customized parts are needed, e.g., medical applications. Furthermore, AM has the potential to reduce material waste further, because material is just added where it is required. In addition to that, no additional tools for manufacturing are required. This is an advantage in comparison to injection molding. Hence, AM can also help to reduce the carbon footprint, because no energy is required to manufacture expensive tools. In general, AM can be divided in seven process categories: Material Extrusion (MEX), Vat-Photopolymerization (VPP), Material Jetting (MJT), Sheet Lamination (SHL), Powder Bed Fusion (PBF), Directed Energy Deposition (DED), and Binder Jetting (BJT) [16, 17]. The main differences regarding the process categories for polymers are in view of the used polymer type, material form, and how the polymer bonding is achieved. When it comes to the process categories MEX and VPP, both include two of the most known AM processes. The most popular AM process regarding MEX is Fused Layer Modeling (FLM) and for VPP Stereolithography (VPP-UVL/P). In FLM, a thermoplastic filament is driven through a heated extruder and deposited on the build platform. On the contrary, VPP-UVL/P uses duroplastic resins, which are scanned by a UV laser to induce crosslinking [14]. The process category PBF includes all AM processes that manufacture a component in a powder bed and initiate the bonding between particles by melting, e.g., with laser light or IR-radiation. Hence, PBF works with a thermal bonding mechanism. Hereby, the material could be a metal or a polymer powder [16, 18]. One of the most known polymer-based PBF processes is laser sintering, called laser-based powder bed fusion of polymers (PBF-LB/P) after DIN ISO ASTM 52900 [16].

During the PBF-LB/P process, the whole build chamber is heated up close to the melting temperature T_m of the polymer, e.g., 10°C below T_m. The laser then supplies the rest of the energy that is needed to melt partially the polymer. Figure 1 depicts a scheme of the PBF-LB/P process. The PBF-LB/P process can be divided into three main steps. In the first step, the recoater deposits a powder layer with a defined layer thickness on the build platform. In the second step, the laser is activated to partially melt the areas of the powder bed where the part should be manufactured. In the third step, the build platform moves downwards with a defined layer thickness, and the cycle of the three steps is repeated until the manufacturing process of the part is finished [11, 19].

The PBF-LB/P market is mainly dominated by polyamides (PA), which make roughly 90% of the current market [20–22]. To be a good alternative to injection molding, it is necessary to have additional polymers available for PBF-LB/P in the future. Therefore, one interesting material is (U)HMWPE because its origin, which is a polyolefin, makes it a commodity polymer, while the resulting properties after processing classify it as an engineering polymer. Furthermore, its polyolefin origin leads to a lower price compared to PA materials [23].

Since a few years, research activities are devoted to the use of (U)HMWPE for PBF-LB/P. Back in 2010, Goodridge et al. [24] started the first feasibility studies for the processing of UHMWPE in PBF-LB/P. For their studies, they used an industrial PBF-LB/P machine from the company 3D Systems of the type Vanguard Laser Sintering machine. The investigated UHMWPE had a narrow sintering window of approximately 10°C. Furthermore, the average particle size was 120 µm, which is larger than the value of other commercial PBF-LB/P powders. An average build temperature of approximately 135°C was suitable for manufacturing UHMWPE specimens. Even if this is close to the melting temperature of 140°C, it reduces problems regarding curling and warpage. By using a double scan count, warpage could be minimized further. However, the high build temperature and energy input, caused by the double scan count, lead to significant thermal expansion of the UHMWPE specimens. In general, an exact adjustment of temperature, time, and processing parameters is necessary to enable successful processing of UHMWPE in PBF-LB/P [24].

In 2019, Khalil et al. [25] investigated a UHMWPE grade on an industrial PBF-LB/P machine from the company EOS of the type FORMIGA P100. It is mentioned that UHMWPE is far from ideal for the PBF-LB/P process because of its narrow sintering window, large particle size, and not perfectly spherical morphology. Anyway, they were able to manufacture specimens of UHMWPE. However, the specimens were highly porous with a rough surface. The authors suggest that processing of UHMWPE could be improved by increasing the bulk density or modifying the particle size, morphology, and the sintering window [25].

As mentioned by Christakopoulos et al. [26] the tensile strength (determined by tensile tests under uniaxial loading) of laser-sintered specimens is lower than for compression-molded specimens. The lower number of entanglements that are formed during the PBF-LB/P is a possible reason for that. In compression molding, the formation of entanglements is more pronounced, which yields higher values of the mechanical properties [26].

Bryant et al. [27] investigated different hatch spacings on a Promaker P2000 HT from the company Farsoon. A lower hatch spacing leads to a higher growth in *z*-direction directly after melting, which could result in a collision with the recoater. Their advice is to use a larger hatch spacing to reduce the growth in *z*-direction. After that the manufactured part should be put in an oven for post-treatment at the melting temperature. The shape of the manufactured part should stay the same because of the high melt viscosity of UHMWPE. Nevertheless, the mechanical properties of those parts are lower than for compression molded parts because of the higher porosity [27].

The objective of this article is to develop a processing strategy and to investigate the influence of carbon black (CB) concentration on the surface of HMWPE powders for PBF-LB/P machines with a diode laser. Diode laser typically have a wavelength of 808 nm, which does not belong to the "fingerprint"-area of polymers [28]. This leads to an insufficient absorption of the wavelength and therefore to an insufficient energy input.

Various methods exist to enhance laser absorption. One method is colloidal additivation, in which polymer particles, such as thermoplastic polyurethane (TPU), are mixed with nanoparticles, such as silver nanoparticles, in a liquid medium. This process results in the adsorption of silver nanoparticles onto the surface. This leads to improved absorption properties in the near-infrared (NIR) spectrum and enabling successful processing via laser sintering [29]. Another established approach is to surface coating the polymer with a material that exhibits high absorption in the relevant spectrum. For instance, coating polyamide 12 (PA 12) with gold nanorods has demonstrated the feasibility of manufacturing via NIR laser sintering [30]. However, both silver and gold are significantly more expensive than alternatives such as CB, graphene, or copper. Initial studies have also explored the use of copper nanoparticles in laser sintering. The results suggest that processing copper nanoparticle-filled polymer systems with diode lasers is feasible [31]. Nonetheless, the addition of metal particles can reduce the specific heat capacity of the material, which in turn increases its thermal conductivity. This change affects the thermal balance during laser sintering [32].

To increase absorption quantitatively, it is possible to add CB to the polymer powder [33], because CB is able to absorb the wavelength of diode lasers in a proper way. This enhances the coupling between the laser energy and the polymer powder, allowing the material to heat and melt effectively during the sintering process. Even if carbon black could reduce the coalescence when reaching a critical concentration [34], the CB particles absorb the laser energy, which increases the temperature of the CB particles. Hence, carbon black works as a heat conductor to melt partially the polymer particles. In addition to its improved energy absorption, CB is well known in the polymer industry as a multifunctional filler. It contributes to UV resistance and can enhance mechanical properties [35]. Furthermore, CB has broadband absorption capabilities and is relatively inexpensive, making it the standard infrared (IR) absorber in many applications [36]. CB is also commonly used in laser transmission welding (LTW) when employing diode lasers. In this context, increasing the CB concentration leads to higher temperatures at the laser spot, attributed to a higher depth-to-width ratio and weld width, both resulting from enhanced absorption properties [37]. At this moment, most results with UHMWPE in PBF-LB/P were achieved by using industrial machines with a CO_2-laser. By developing a processing strategy for diode laser based PBF-LB/P machines it could be possible to make (U)HMWPE accessible for a wider audience.

TABLE 1 | Investigated powder mixtures.

Powder mixture	CB concentration [wt.%]
GUR 4118-Virgin	0.00
GUR 4118-CB(0.25)	0.25
GUR 4118-CB(0.5)	0.50
GUR 4118-CB(1)	1.00
GUR 4118-CB(2.5)	2.50

2 | Experimental Methods

2.1 | Materials

The HMWPE used in this study was GUR 4118 (Celanese, Frankfurt am Main, Germany). The virgin GUR 4118 has a viscosity average molecular weight M_v of 6×10^5 g mol^{-1} [38]. Moreover, the carbon black used in this study was KLAREX RG 225 (Himadri, India), which was supplied by Weber & Schaer (Hamburg, Germany).

The GUR 4118 was dry-blended with different weight concentrations of CB by putting both materials in a bucket and subsequently shaking for 5 min. The investigated powder mixtures are shown in Table 1. The pristine GUR 4118 is used as reference (GUR 4118-Virgin).

2.2 | Powder Properties

The combination of optical microscopy and the image software ImageJ is used to determine the particle morphology, the circularity, and the particle size distribution, respectively. The used light stereo microscope was manufactured by OLYMPUS type DSX 500. The lens used has a 50x magnification. Particles of each powder mixture were placed on the object desk. To record at least 100 particles for each powder mixture, microscopic images were recorded at different positions. The software ImageJ converted the recorded images to a black white image. Care was taken that the particles were separated from each other in order to measure the circularity and particle size for each particle.

The bulk density of the powder mixtures is determined after DIN EN ISO 60 [39]. 110 mL of the powder mixture was filled in the funnel and then flowed into a cup with a volume of 100 mL. Afterwards, the mass of the powder in the cup was measured to determine the bulk density. The measurement is done three times for each powder mixture.

2.3 | Fourier Transform Infrared-Spectroscopy

The investigation of the optical properties and Fourier transform infrared (FT-IR) spectra in the attenuated total reflection (ATR) mode of compression molded parts with different carbon black concentrations was determined using an FT-IR spectrometer Frontier (Perkin Elmer, Massachusetts, USA). For the measurements, 64 scans were collected and averaged with a resolution of 4 cm^{-1} in a wavenumber range from 4000 to 650 cm^{-1}. All measurements were carried out at room temperature.

2.4 | Differential Scanning Calorimetry

A differential scanning calorimetry (DSC) apparatus (type DSC 8000 of Perkin Elmer, Massachusetts, USA) was used to determine the sintering window of the different powder mixtures. Therefore, one heating and one cooling cycle were performed. The measurements were performed in a nitrogen atmosphere, and the mass of the powder was approximately 5 mg. A temperature range from 30 to 190°C was chosen for the investigations. At the start and the end temperatures a holding time of 5 min was chosen to reach thermal equilibrium. The used heating and cooling rates were both 10 K min^{-1}.

Since the carbon black might change the thermal behavior during the process and affect the temperature distribution, the specific heat capacity c_p of the powder mixtures was determined in accordance to DIN EN ISO 11357-4 [40]. The investigated temperature range was also from 30°C to 190°C with a heating rate of 10 K min^{-1}.

2.5 | Rheological Experiments

The rheological experiments were carried out in shear using a rotational rheometer (Kinexus Ultra+, Netzsch, Selb, Germany). Cylindrical samples with a diameter of 8 mm and a thickness of 1 mm were prepared by compression molding at a temperature of 200°C and a compression time of 6 min. The frequency sweeps were carried out at a temperature of 150°C. After insertion of the samples, a time interval of 5 min was chosen for thermal equilibration. The gap was set by using an initial normal force of 0.5 N for 1 min to realize complete contact between the plates. To determine the linear viscoelastic regime, stress sweeps at an angular frequency ω of 10 rad s^{-1} were carried out between 100 and 10 000 Pa. Frequency sweeps were subsequently performed in the range of angular frequencies from 0.01 to 100 rad s^{-1} (starting with the highest frequency) with a stress amplitude of 1000 Pa. All tests were carried out in a nitrogen atmosphere.

2.6 | Mechanical Properties and Coalescence of Laser-Sintered Parts

Tensile tests under uniaxial loading with tensile bars of type 1BA were carried out to determine the mechanical properties. For the tensile tests, a test rig from Shimadzu type EZ-SX with a force transducer of 5 kN was used. The crosshead speed was 1.2 mm min^{-1}, which is equal to a strain rate of approximately 2 % min^{-1}. The nominal strain rate was determined by taking the movement of the crosshead into account. The nominal stress σ was calculated by dividing the measured force by the initial cross-sectional area of the sample. All tensile tests were done under ambient conditions (room temperature). The Young's modulus E is determined after DIN EN ISO 527-1 in the strain interval from 0.05% to 0.25% [41].

The degree of coalescence Y_c is analyzed using optical micrographs of the cross-sectional area of the tensile bars and the equation [42]

$$Y_c = 2L_c/(P_1 + P_2) \tag{1}$$

Hereby, L_c describes the contact length between two neighboring particles. The variables P_1 and P_2 are the perimeters of the particles. For the investigations, 20 particle collectives were tested.

For additional validation of the melting result, the porosity of the cross-sectional area P_A is determined by analysing the fracture area of optical micrographs using ImageJ. To achieve this, the total fracture area A_C is measured and the sum of the pore areas A_P is determined. Then the cross-sectional area P_A follows from

$$P_A = \frac{A_P}{A_C} \cdot 100\% \tag{2}$$

2.7 | PBF-LB/P System

Processing of the powder mixtures was carried out on a PBF-LB/P system of the type Lisa (Sinterit, Krakau, Poland). The Lisa apparatus has a print bed size of 150 × 200 × 150 [mm] and the build chamber can be heated up to 210°C. Moreover, the piston, feed bed, and print bed can be heated up to reduce thermal gradients. With this device, it is possible to use layer thicknesses between 0.75 and 200 µm. For the powder deposition during the process, Lisa uses a counter-rotating roller recoater. In terms of the laser system, Lisa uses a diode laser with a power of 5 W and a wavelength of 808 nm [43]. Hence, it is necessary to add CB to GUR 4118 since polymers are only able to absorb the wavelength of 808 nm to a large extent with additivation. One of the typical additives to improve the absorption of polymer powders is carbon black [15].

The general processing of the powder mixtures was first tested using GUR 4118-CB(0.25). The laser power of the machine was fixed at 5 W. Therefore, changes in the volume energy density

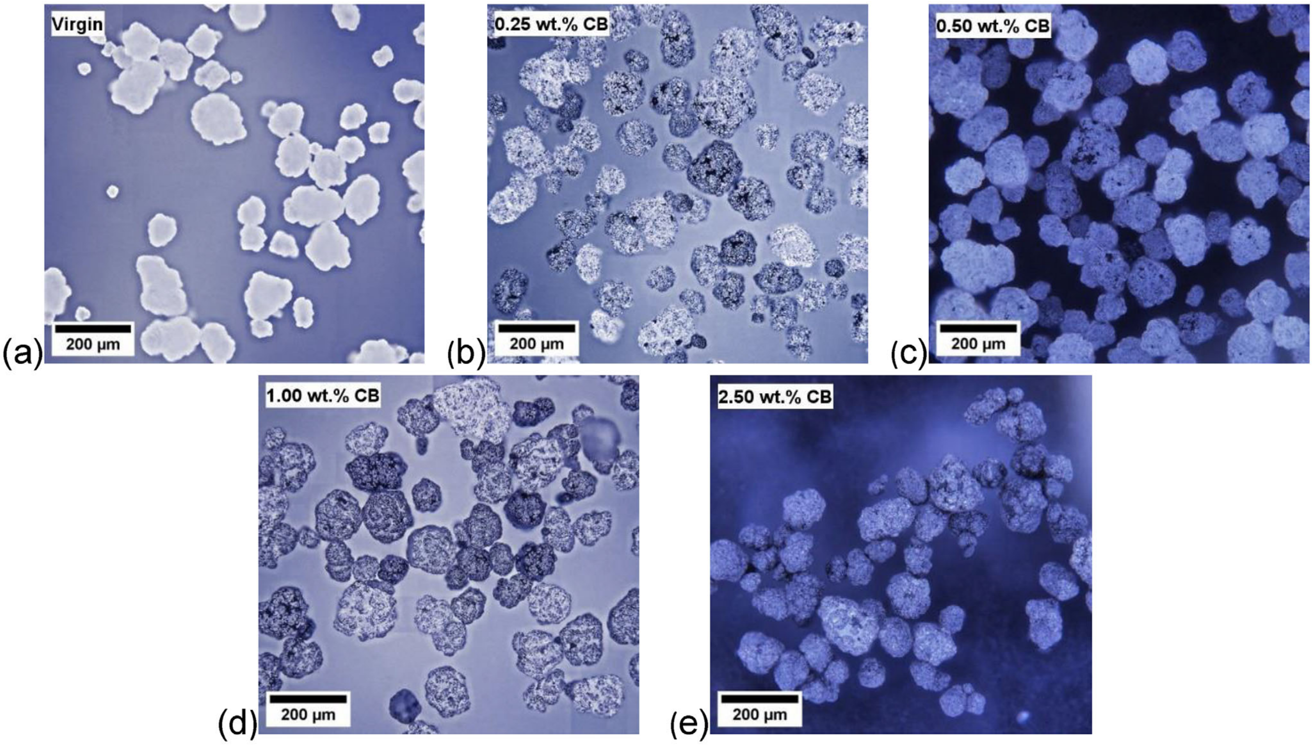

FIGURE 2 | Optical micrographs of the powder mixtures with a carbon black concentration of (a) 0.00, (b) 0.25, (c) 0.50, (d) 1.00, and (e) 2.50 wt.%.

were achieved by adjusting the scan speed. For the initial laser sintering trials, a constant layer thickness of 125 µm and a hatch spacing of 0.3 mm were used, with a volume energy density of 260 J cm^{-3}. This corresponds to a scan speed of 512.8 mm s^{-1}. The main objective of these initial trials was to identify suitable processing temperatures, which would then serve as a basis for further optimization of the processing parameters. A temperature range of 130°C–135°C (in 1°C increments) was investigated using job layout (a). After determining the appropriate processing temperatures, job layout (b) was tested using the same parameters as layout (a), with the aim of evaluating whether the reduced scanning area could help minimize curling (both job layouts are depicted in Figure 9). Additionally, qualitative trials were conducted with layout (b), using a layer thickness of 200 µm and hatch spacings of 0.2 mm and 0.3 mm, at the same constant energy density of 260 J cm^{-3}. These tests aimed to assess the influence of layer thickness and hatch spacing on curling behaviour and to prevent curling during further processing. The final laser sintering trials were conducted at a print bed temperature of 135°C and a chamber temperature of 134°C, with a hatch spacing of 0.2 mm and a layer thickness of 200 µm. Four volume energy densities, 260, 340, 420, and 500 J cm^{-3} were tested, corresponding to scan speeds of 480.8, 367.7, 297.6, and 250.0 mm s^{-1}, respectively.

3 | Results and Discussion

3.1 | Particle Morphology and Size Distribution

The particle size distribution and the particle morphology play a key role for a successful PBF-LB/P process. The typical particle size of commercial PBF-LB/P materials ranges between 20 and 80 µm [44, 45]. Hereby, the content of smaller particles should not be too high since it could cause some agglomeration of the particles and hence lead to problems during recoating [15, 45, 46]. Regarding the circularity of the particles, this should be as high as possible since it leads to a higher powder density [15, 46–48]. The CB particles adhere to the surface of the GUR 4118 powder particles. Hereby, the distribution of the CB particles is inhomogeneous (Figure 2), which could lead to non-uniform melting of the particles, since a higher CB concentration yields a more pronounced absorption of laser energy.

The cumulative particle size distribution increases with increasing carbon black concentration. The carbon black particles on the surface of the GUR particles shift the particle size distribution to higher values (Figure 3a). In general, the particle size of each powder mixture is larger than the typical particle size for PBF-LB/P. For each powder mixture, the d_{90} value is larger than 100 µm. Consequently, a layer thickness larger than 100 µm is necessary. Typically, laser sintering machines can accommodate a range of layer thicknesses, e.g., 75 to 200 µm, so powders with particle sizes larger than 100 µm are generally suitable. In addition to that, the circularity of the particles remains almost constant, whereas the bulk density increases up to a defined CB concentration (Figure 3b) and decreases for higher CB concentrations. The bulk density shows a significant increase by adding 0.25 wt.% CB. Hereby the smaller CB particles could fill possible voids between larger particles. This leads to denser powder layers during the PBF-LB/P. By increasing the CB concentration up to 1.00 wt.% the bulk density decreases, but is still higher than for the virgin powder. With further increase of the CB concentration, the bulk density decreases to a value that is smaller than for the virgin powder. In that case, the CB yields a higher tendency for agglomeration, which results

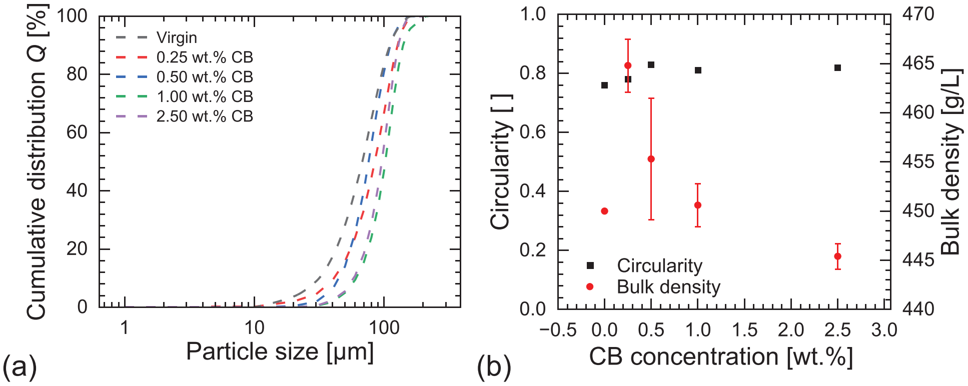

FIGURE 3 | Particle size distribution and circularity: (a) Cumulative particle size distribution and (b) circularity and bulk density as a function of carbon black concentration.

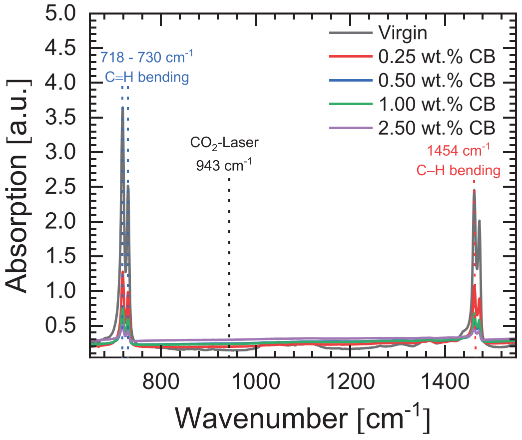

FIGURE 4 | Absorption as a Function of Wavenumber for the Different Carbon Black Concentrations.

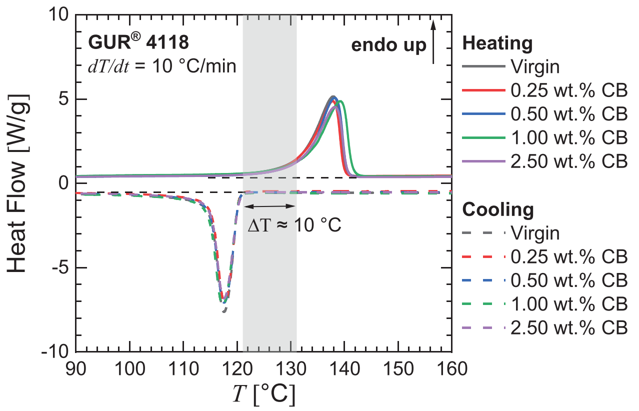

FIGURE 5 | Results of DSC measurements (heat flow as a function of temperature), which reveal the sintering window for the different carbon black concentrations.

in more voids. The bulk density is a function of the density of the single particles (i.e. approximately the density of HMWPE) and the density of CB, as well as porosity. Since porosity is a complex function of the sizes and the flow behaviour of HMWPE particles and CB, as well as the CB distribution, the data appear reasonable.

3.2 | Optical Properties

The addition of carbon black increases the absorption of the powder mixtures for processing in PBF-LB/P (Figure 4). The FT-IR spectrum shows an increase of absorption at 943 cm^{-1} with increasing carbon black concentration. The corresponding wavenumber of a diode laser is at 12376 cm^{-1}. This wavenumber is not covered by the FT-IR device. However, the tendency shows that the absorption is increased for each wavenumber except the ones where the characteristic polyethylene peaks appear (e.g., at 1454 cm^{-1}) [49–51]. According to the literature, CB shows a high absorption in the relevant wavelength range from 800 to 950 nm and increases with increasing CB concentration [52]. Therefore, it can be assumed that the absorption is also increased in the wavenumber range of the diode laser.

3.3 | Sintering Window and Specific Heat Capacity

One key parameter for PBF-LB/P is the so-called sintering window. The sintering window describes the temperature difference between the onset temperature for melting and crystallization [15, 45, 53]. The addition of carbon black only has a marginal impact on the sintering window because it has no impact on the molecular level. The sintering window for all powder mixtures is approximately 10°C and hence very narrow (Figure 5). For comparison, polyamide 12 (PA 12) has a sintering window in the order of 25°C to 30°C [45, 54]. Moreover, the crystallization temperature strongly depends on the cooling rate. For lower cooling rates, the crystallization temperature is shifted to higher temperatures [15]. During the PBF-LB/P no constant heating or cooling rates appear in comparison to DSC measurements. Therefore, the sintering window during PBF-LB/P presumably is even smaller. To achieve a high coalescence of polymer particles and a high adhesion between the sintered layers, crystallization should be inhibited as long as possible [15, 45, 53]. If crystallization starts to early, then curling and warpage occur, which could lead to a potential collision between sintered layers and the recoater. Hence, selection of the optimum temperature and realization of a mostly spatially uniform temperature distribution are essential for successful processing of the powder mixtures.

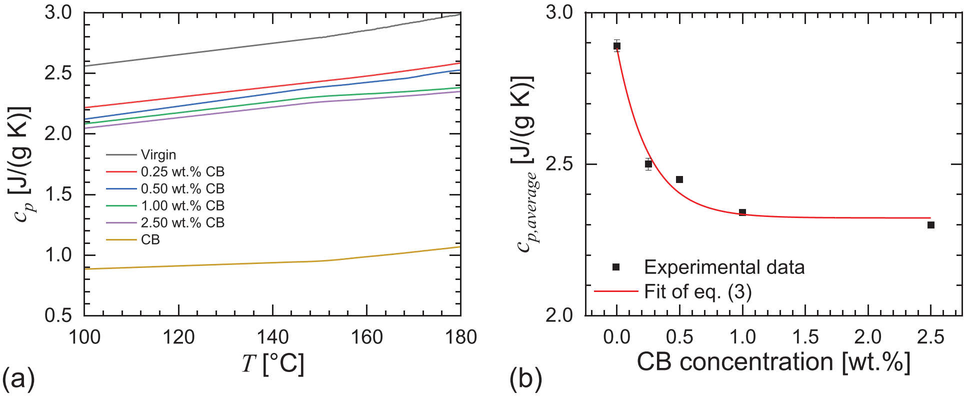

FIGURE 6 | (a) Specific heat capacity $\boldsymbol{c_p}$ dependent on temperature and carbon black concentration, and (b) specific heat capacity dependent on carbon black concentration for the temperature range from 160 to 170°C. The red line in (b) is a fit of Equation (3).

The increased carbon black concentration leads to a lower capability of storing heat, because the thermal conductivity of the carbon black is higher than for the virgin GUR 4118. The specific heat capacity decreases with increasing carbon black concentration (Figure 6a). Thus, it can be assumed that the thermal conductivity increases with the carbon black concentration. This could affect the processing results in a way that the temperature distribution becomes more inhomogeneous and yields a more unstable process. The general relationship between the specific heat capacity and the CB weight concentration w (Figure 6b) for the investigated concentration range can be described by an exponential function:

$$c_{p,\mathrm{CB}} = c_{p,\mathrm{GUR}} + 0.56\,\frac{\mathrm{J}}{\mathrm{gK}} \times \exp\left(-4w\right) \tag{3}$$

3.4 | Rheological Properties

The low CB concentrations do not affect the particle coalescence. Generally, the storage and the loss moduli G' and G'' of the pure HMWPE and the composites decrease with decreasing angular frequency ω and attain similar values, such that the loss tangent $\tan\delta$ does not vary much with ω. A higher CB concentration only has a minor effect on the rheological properties for the investigated concentrations and attains similar values for each CB concentration within statistical scatter (Figure 7a,b). The average relaxation time τ can be roughly estimated by the crossover-frequency of 1.585 rad s^{-1} for each concentration, which corresponds to an average relaxation time of approx. 0.63 s. The terminal zone of the Maxwell model is not attained in the investigated range of frequencies. On the contrary, the complex shear viscosity decreases with ω with the power-law $|\eta^*| \propto \omega^{-0.5}$, independent of the CB concentration (Figure 7c). According to the literature, the rheological properties of polymers start to be affected by the CB concentration only at much higher concentrations of around 5 to 10 vol.%, respectively [55, 56].

One of the earliest attempts to propose particle coalescence in PBF-LB/P was made by the model of Frenkel-Eshelby:

$$\frac{y}{r} = \left(\frac{\Gamma t}{\eta_0}\right)^{\frac{1}{2}} \tag{4}$$

This model correlates the half neck radius y and the particle radius r with the surface tension Γ, the time t, and the zero shear rate viscosity η_0. Therefore, the complex shear viscosity at low frequencies is one of the key properties for a fast coalescence. Hereby, a higher magnitude of complex shear viscosity leads to a slower coalescence and, thus in general, a weaker bonding between particles and laser-sintered layers during the manufacturing process. The zero shear rate viscosity η_0 cannot be determined in the investigated frequency range for the polymer/powder mixtures (Figure 7c). As the viscosity increases with decreasing frequency, it can be assumed that the zero shear rate viscosity of each powder mixture is higher than the experimental data at 0.01 rad s^{-1}. For comparison, PA 12 has a zero shear rate viscosity in the order of 1000 Pa s (depending on molecular weight and temperature) [57] and hence at least three decades lower than the zero shear rate viscosity of HMWPE. This is one of the major challenges, besides its narrow sintering window, of HMWPE for processing by means of PBF-LB/P.

3.5 | PBF-LB/P Processing

An increased powder bed temperature inhibits the re-crystallization for a longer time. Therefore, the tendency to curl is slightly reduced (Figure 8), cf. the work of Mousa et al. [58] In the temperature range between 130°C and 133°C no sufficient bonding between sintered layers is achieved. The tendency to curling is too high and leads to displacements of the sintered layers, because of collisions with the recoater. A further increase of print bed temperature, above 135°C, was not tested. The reason was that 135°C is already outside the sintering window of the powder mixture and near the melting peak. A further increase contains the danger that a high amount of powder could melt. However, even at a print bed temperature of 135°C, some curling and insufficient fusion of the powder remain, which also leads to an insufficient bonding between adjacent layers (Figure 8f). This indicates that the cooling rates during the process are low enough that even at a temperature of 135°C re-crystallization could occur and that the energy input is not high enough to create a sufficient interlayer bonding. Especially previously printed layers will have a lower temperature than the top layer of the print bed, which leads to the fact that re-crystallization starts even faster, and the manufactured layers tend to curl and

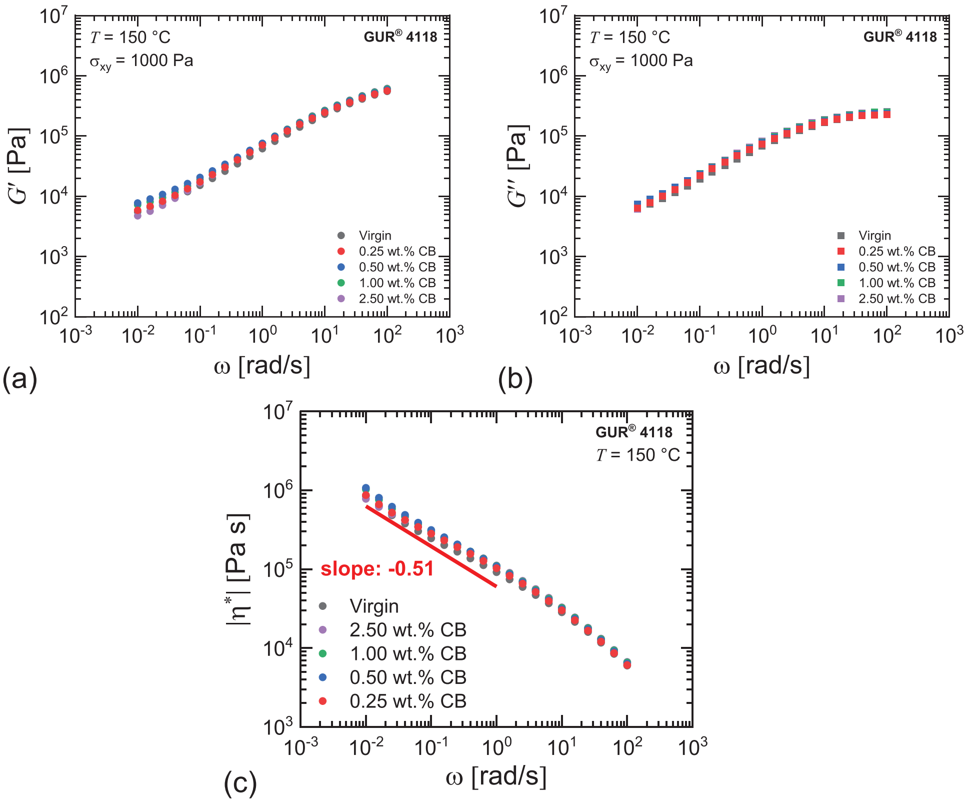

FIGURE 7 | Dynamic moduli $G'(\omega)$, $G''(\omega)$ and magnitude of complex shear viscosity $|\eta^*|$ measured in frequency sweeps at a temperature of 150°C with a stress amplitude of 1000 Pa for the different carbon black concentrations. (a) Storage modulus G', (b) loss modulus G'' and (c) magnitude of complex viscosity $|\eta^*|$.

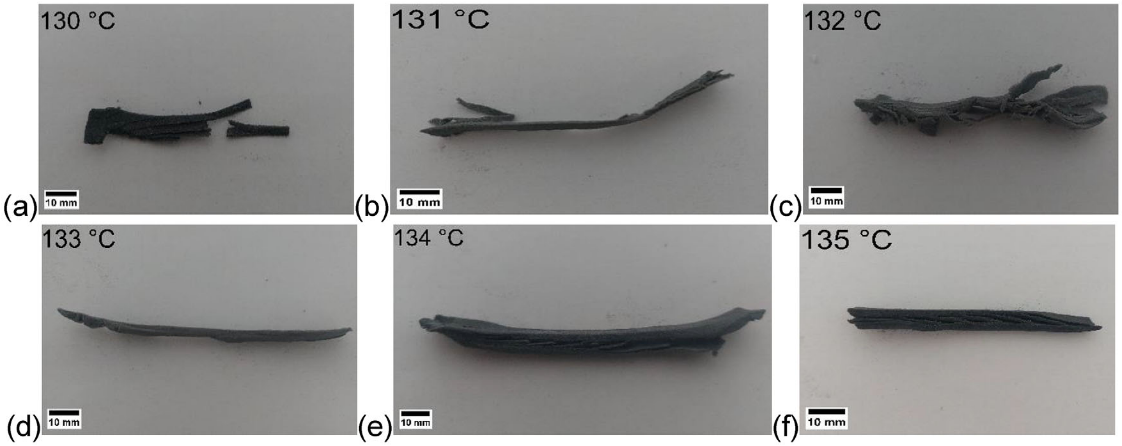

FIGURE 8 | Photography of laser-sintered specimens for different print bed temperatures by using job layout (a), hatch spacing of 0.3 mm, and layer thickness of 125 µm.

delaminate. To overcome the problems of curling and insufficient bonding between layers, the scanning area is reduced by using job layout (b) (Figure 9b). Since the initial trials showed that even at 135°C, curling occurs for job layout (a), job layout (b) was just tested at this temperature.

The reduced scanning area leads to a stronger bonding between the layers, since there are no voids between them (Figure S1). The energy input is high enough to form a sufficient interlayer bonding, since the energy input per area is increased. Nevertheless, curling still occurs. To reduce the curling further, the layer thickness was changed to 200 µm and the hatch spacing to 0.2 mm. The decreased hatch spacing causes a higher energy input, which in general should lead again to a higher temperature and inhibit the re-crystallization for a longer time. The increased layer thickness reduces the collision potential between the sintered layers and the recoater. Even if a certain degree of curling is present, the probability of sintered layers protruding from the powder bed is reduced due to the higher layer thickness. The laser sintering of specimens with a layer

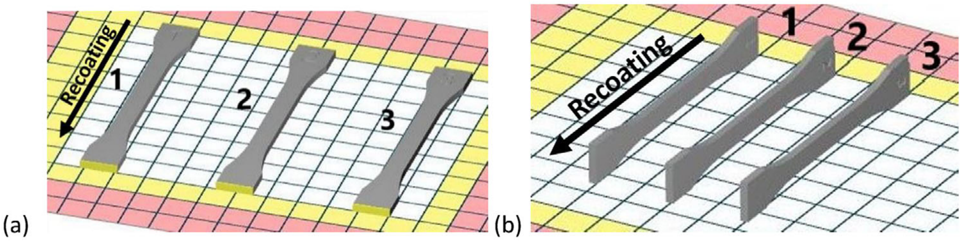

FIGURE 9 | Investigated job layouts (a) and (b).

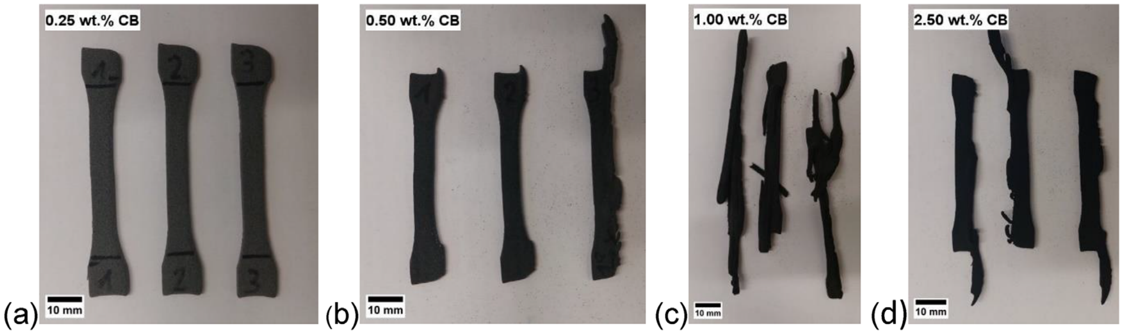

FIGURE 10 | Photography of PBF-LB/P manufactured tensile bars with a carbon black concentration of (a) 0.25, (b) 0.50, (c) 1.00, and (d) 2.50 wt.%.

thickness of 200 µm and a hatch spacing of 0.2 mm was in general, successful (Figure 10). The CB concentration significantly effects the laser sintering result. An increase of CB concentration leads to a reduced processability (Figure 10). Especially at CB concentrations of 1.0 and 2.5 wt.% the tensile bars show deviations from the target geometry. For these tensile bars, it is not possible to perform tensile tests because of the geometrical deviation. Even for GUR 4118-CB(0.5) it can be observed that one tensile bar shows defects. It appears that pre-sintered layers are somehow colliding with the recoater and becoming displaced within the powder bed. However, no recoating defects, such as stripes in the powder bed caused by the movement of agglomerates, were observed. Only the processing using a CB concentration of 0.25 wt.% leads to tensile bars in sufficient quality. Even if a small degree of curling remains, the bonding between the layers is high enough that no empty voids between them can be observed. The reason for the observed defects could be the lower specific heat capacity for higher CB concentrations. This could lead to a faster cooling/discharging of the heat of laser-sintered layers and lead to an earlier re-crystallization, which results in curling. Those curled layers would collide with the recoater and be ripped out of the powder bed, which could lead to the observed defects at the tensile bars (Figure 10b–d). Another possible reason could be an increased expansion of the material in the build direction. Investigations of UHMWPE with different hatch spacings showed that this expansion becomes stronger when the hatch spacing decreases and is directly connected to the peak temperature [27]. A smaller hatch spacing corresponds to a higher energy input/temperature, because the overlapping of laser traces becomes larger. A higher CB concentration also leads to a higher peak temperature, because of the higher laser absorption [37]. This could also lead to an increased expansion in build direction, shortly after laser exposure, and therefore an increased potential of collisions between the recoater and sintered layers.

To estimate this effect of the specific heat capacity, the thermal conductivity $\lambda_{i,\mathrm{CB}}$ of the powder mixtures with the concentration i is calculated by using the rule of mixture [59]:

$$\lambda_{i,\mathrm{CB}} = (1 - \Phi)\,\lambda_{\mathrm{HMWPE}} + \Phi\lambda_{\mathrm{CB}} \tag{5}$$

Hereby λ_{HMWPE} and λ_{CB} are the thermal conductivity of HMWPE and carbon black, respectively. According to the literature, the value of λ_{HMWPE} is approximately 0.41 $\mathrm{W\ m^{-1}K^{-1}}$ and the one of λ_{CB} is 0.908 $\mathrm{W\ m^{-1}K^{-1}}$ [60, 61]. The volume fraction Φ is calculated using

$$\Phi = \frac{w\rho_{\mathrm{HMWPE}}}{w\rho_{\mathrm{HMWPE}} + (1 - w)\,\rho_{\mathrm{CB}}} \tag{6}$$

The used values for the densities are 950 $\mathrm{kg\ m^{-3}}$ for ρ_{HMWPE} and 2000 $\mathrm{kg\ m^{-3}}$ for ρ_{CB} according to the supplier.

The thermal diffusivity $a_{i,\mathrm{CB}}$ is calculated by taking into account the thermal conductivity, the specific heat capacity $c_{p,i,\,\mathrm{CB}}$ (Figure 6b) and the density of the powder mixture $\rho_{i,\mathrm{CB}}$:

$$a_{i,\mathrm{CB}} = \frac{\lambda_{i,\mathrm{CB}}}{\rho_{i,\mathrm{CB}}c_{p,i,\mathrm{CB}}} \tag{7}$$

Hereby, the density of the powder mixtures is also estimated by using the rule of mixture. Equation (7) implies that the thermal diffusivity increases by approximately 10% from 0.25 to 2.5 wt.% CB (Figure 11). Even if this increase in the time scale of temperature decay does not seem high, in the case of the investigated HMWPE powder, every temperature deviation could have a significant impact on the processing result, because of its narrow sintering window. This simplified approach shows that selecting an adequate CB concentration is important, because on the one hand, the absorption increases (and hence melting

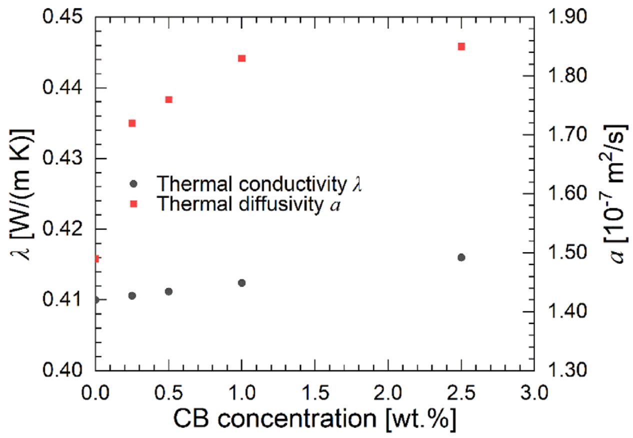

FIGURE 11 | Thermal conductivity and resulting thermal diffusivity $\boldsymbol{a_{i,CB}}$ (Equation 7) after melting, and a constant time dependent on the carbon black concentration.

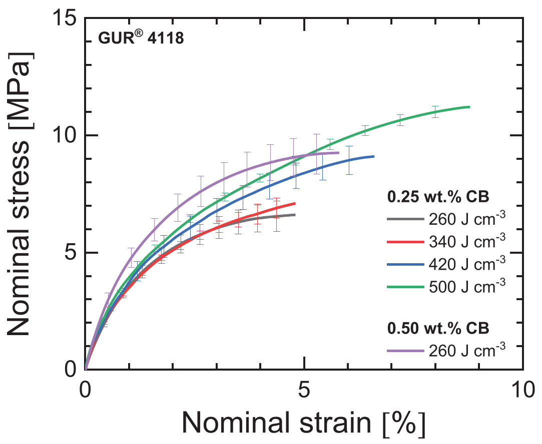

FIGURE 12 | Nominal stress-nominal strain diagram for the manufactured tensile bars dependent on volume energy density $\boldsymbol{E_v}$ and carbon black concentration.

proceeds more rapidly), and on the other hand, a too high concentration affects the processing result.

3.6 | Mechanical Properties and Coalescence

A higher volume energy density E_v leads to a stronger bonding between powder particles and adjacent layers. Thus the Young's modulus, nominal stress, and strain at break increase with increasing volume energy density (Figures 12 and 13). Hereby, a nearly linear dependency between the mechanical quantities and the volume energy density is observed. Experimental and numerical investigations have shown an almost linear relationship between energy input and the dimensions of the laser trace or weld. As the energy input increases, the laser trace becomes wider [37]. In the case of PBF-LB/P, this leads to an increased overlap of scan lines at a constant hatch spacing. As a result, more powder is melted, which contributes to improved mechanical properties. All tensile bars show brittle fracture behavior and therefore, the tensile strength corresponds to the stress at break. The brittle behavior of the specimens results from the layerwise manufacturing process and the remaining porosity. Moreover, the mechanical properties are affected by the part position in the print bed and the distribution of the CB particles. Both affect the energy input. The influence of the part position can be seen by the values of the standard deviation (Figure 12) and the exact nominal stress-nominal strain curve for each tensile bar in the (Figure S2). The position dependency of the mechanical properties results from two reasons. The first reason is that the temperature distribution is not spatially uniform, which results in different temperatures on top of the powder bed. Consequently, melting is more complete in areas where the powder bed temperature is higher. The second reason is that the energy input also depends on the shape of the laser spot. Typically, the spherical shape of the laser spot is reached exactly when the laser spot meets the center of the print bed. The deflection of the laser spot due to the mirror movement changes its shape. This leads to a more ellipsoidal shape when the laser spot is moved away from the center. This ellipsoidal shape has a higher area than the spherical shape and therefore, the energy density is lower for parts that are not in the center of the print bed. The absorption properties of the powder have a higher impact on the mechanical properties than the pure energy input. The different absorption properties (Figure 4) lead to differences in the mechanical properties, because the melting process is influenced by the absorbed laser energy. A higher CB concentration increases laser absorption and, consequently, raises the melt temperature. According to the literature, the peak temperature also shifts toward the interface of the absorbing material [37]. This promotes stronger bonding between adjacent layers and particles, as the decreased viscosity at elevated temperatures favors coalescence. With constant volume energy density, the mechanical properties increase with increasing CB concentration (Figure 12). To achieve mechanical properties similar to 0.50 wt.% CB the volume energy density for 0.25 wt.% CB needs to be increased up to 420 J cm^{-3}.

A strong fusion of particles is one of the key factors to achieve high mechanical properties. In general, complete coalescence is not achieved during PBF-LB/P but the formation of so-called sintering necks [15, 42, 45, 62]. The formation of the sintering necks influences the density of the manufactured parts and consequently has an impact on the mechanical properties [15, 45]. Since every tensile bar shows a brittle behavior, it can be assumed that the interphase between neighboring particles is weak because of pores and only partial interdiffusion of polymer chains. The volume energy influences the degree of coalescence as well as the remaining porosity. Hereby, the degree of coalescence slightly increases with increasing volume energy density (Figure 13). The optical micrographs (Figure 14) reveal that no complete coalescence is achieved. With decreasing volume energy density, the general morphology of the powder particles remains. In addition, the degree of porosity is visualized by the voids (red circles) in the optical micrographs. Moreover, with the assumption that the volume of the tensile bars only slightly changes, the mass can be used as an indicator for the density. The mass increases with increasing volume energy density (Figure 15), and the porosity of the cross-sectional area decreases with increasing volume energy density. The low degree of coalescence and high porosity result from the dominant elastic properties/high melt viscosity of the polymer itself.

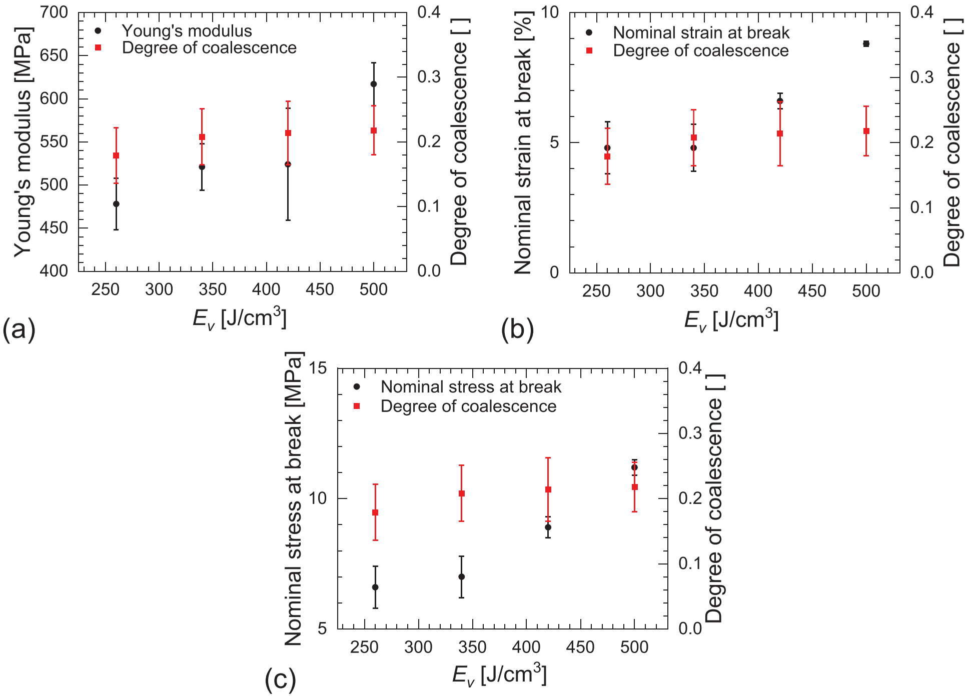

FIGURE 13 | Dependency of the mechanical properties and degree of coalescence of laser-sintered tensile bars of GUR 4118-CB(0.25) on volume energy density: (a) Young's modulus, (b) strain at break, and (c) stress at break.

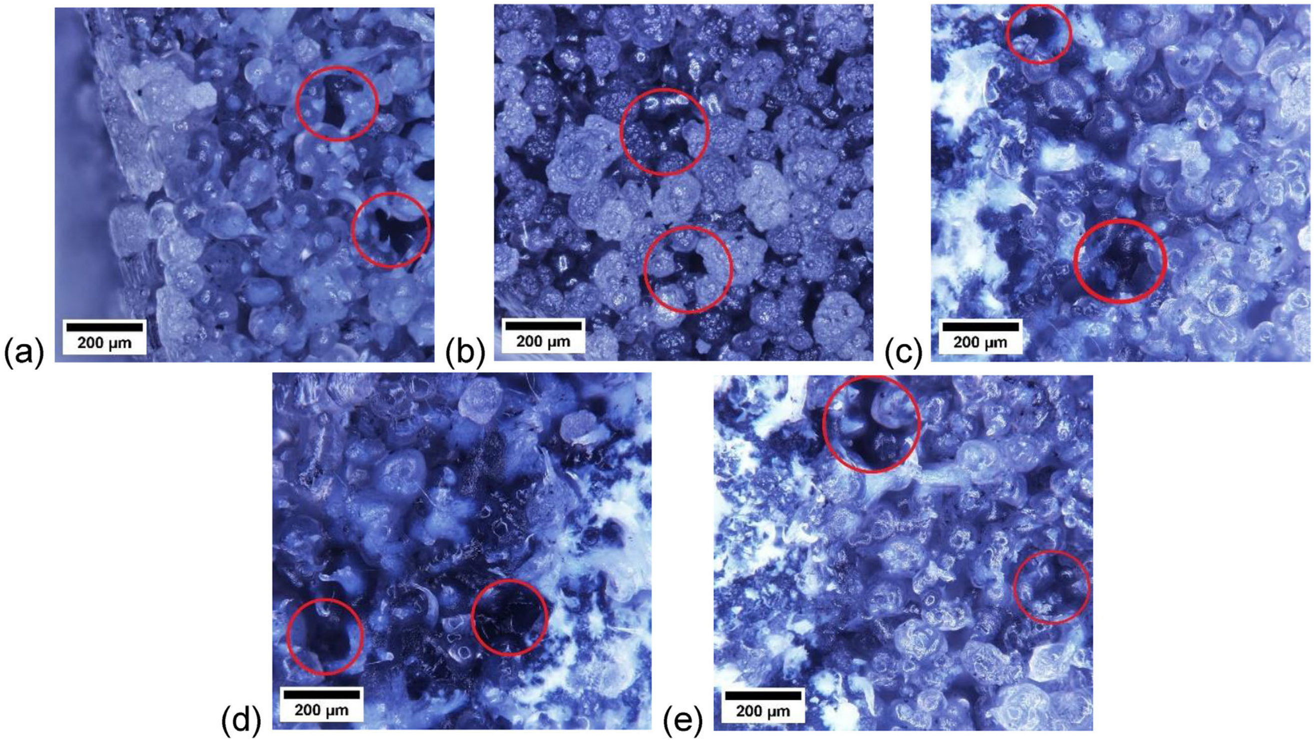

FIGURE 14 | Optical micrographs of the cross-sectional area of the tensile bars for (a) GUR 4118-CB(0.25) and (b) GUR 4118-CB(0.5). The volume energy density $\boldsymbol{E_v}$ is (a) 260 $\mathbf{J\ cm^{-3}}$, (b) 260 $\mathbf{J\ cm^{-3}}$, (c) 340 $\mathbf{J\ cm^{-3}}$, (d) 420 $\mathbf{J\ cm^{-3}}$ and (e) 500 $\mathbf{J\ cm^{-3}}$.

4 | Conclusions

In this work, the impact of carbon black (CB) concentration on an HMWPE powder for processing via diode laser-based PBF-LB/P machines was investigated. The general processing was successful. The results reveal that CB concentration slightly affects the powder properties and significantly affects processing. The tendency of agglomeration of the CB leads to an increase of particle size and a decrease regarding the bulk density if the concentration exceeds 0.25 wt.%. Hereby, the particle size of each

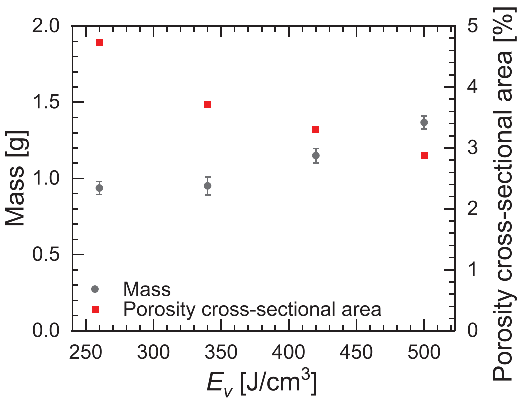

FIGURE 15 | Measured average mass and porosity of PBF-LB/P manufactured tensile bars as a function of volume energy density E_v.

powder mixture exceeds 100 µm and is larger than for typical PA 12 powders for PBF-LB/P. However, compared to the virgin HMWPE, the bulk density increases with adding 0.25 wt.% CB, because the CB particles seem to fill possible voids between the polymer particles. Due to changes in specific heat capacity and thermal conductivity, thermal balance during processing decreases with increasing carbon black concentration. This could promote earlier recrystallization at higher CB concentrations, as heat transfer occurs more rapidly, leading to recoater collisions with curled layers. Notably, the narrow sintering window of HMWPE of 10°C increases the risk of curling and defects if the temperature field is not as homogeneous as possible. Regarding the sintering window, no effect of the CB concentration is observed. The low CB concentrations do not affect the rheological properties. Each powder mixture shows pronounced elastic behavior in the investigated frequency range, which affects the coalescence and melt pool during processing. This behaviour is responsible for the incomplete coalescence, rest porosity, and brittle behaviour of the laser-sintered parts. The processing of the HMWPE powder shows that a suitable processing temperature is at around 135°C. This temperature already exceeds the sintering window of the HMWPE. However, at this temperature, which is close to the upper limit of the sintering window, significant curling problems occur during processing. Future investigations of the isothermal crystallization behaviour as well as DSC experiments with different cooling rates, will help to understand these problems in more detail. A smaller scanning area and larger layer thickness help to mitigate the issues of curling further. Changing the orientation of the part from an XYZ to an XZY orientation significantly reduces curling and increases the interlayer bonding. Based on the investigations, the most suitable CB concentration was determined to be 0.25 wt.%. An increase of the CB concentration above 0.50 wt.% is not recommended because of the observed processing defects. So far, one possible explanation for the reduced processability with increasing CB concentration could be the increased thermal inbalance, because of the changed specific heat capacity as well as the very narrow sintering window. Particle coalescence and interlayer bonding are influenced by volume energy density, both of which improve as the volume energy density increases, leading to enhanced mechanical properties. However, all specimens exhibited brittle fracture behaviour. The high melt viscosity resulted in very porous manufactured specimens. A qualitative comparison also indicated that the mechanical properties are more affected by the absorption characteristics of the powder mixture than by the raw energy input for the chosen test parameters. Overall, this study has provided suitable process parameters, strategies, and CB concentrations as a starting point for further research of HMWPE in PBF-LB/P. For other polymers than HMWPE a CB concentration between 0.25 and 0.50 wt.% could be suitable, too. However, determining the sintering window and the specific heat capacity should always be done to analyse how sensitive the polymer reacts to temperature.

Author Contributions

Christopher Krüsener: Investigation, writing – original draft, methodology, formal analysis, conceptualization. **Ulrich A. Handge**: conceptualization, writing – review & editing, supervision.

Acknowledgements

The authors thank Mr. Pascal Brech, Mr. Julian Dührkoop, and Mr. Diptesh Mukeshbhai Sojitra for experimental support. They are also grateful to Celanese (Frankfurt am Main, Germany), especially to Dr. Rainer Walkenhorst, for providing the GUR 4118 grade and to Weber and Schaer (Hamburg, Germany) for providing carbon black.

Conflicts of Interest

The authors declare no conflicts of interest.

Data Availability Statement

The data that support the findings of this study are available from the corresponding author upon reasonable request.

References

1. K. Patel, S. H. Chikkali, and S. Sivaram, "Ultrahigh Molecular Weight Polyethylene: Catalysis, Structure, Properties, Processing and Applications," *Progress in Polymer Science* 109 (2020): 101290.

2. A. Bistolfi, F. Giustra, F. Bosco, et al. *Journal of Orthopaedics* 25 (2021): 98–106.

3. O. K. Muratoglu, C. R. Bragdon, D. O. O'connor, et al., "Unified Wear Model for Highly Crosslinked Ultra-High Molecular Weight Polyethylenes (UHMWPE)," *Biomaterials* 20 (1999): 1463–1470.

4. S. M. Kurtz, *UHMWPE Handbook: Ultra-High Molecular Weight Polyethylene in Total Joint Replacement* (Academic Press, 2004).

5. C. Bucknall, V. Altstädt, D. Auhl, et al., "Structure, Processing and Performance of Ultra-High Molecular Weight Polyethylene (IUPAC Technical Report). Part 1: Characterizing Molecular Weight," *Pure and Applied Chemistry* 92 (2020): 1469–1483.

6. A. Y. Malkin, T. A. Ladygina, S. S. Gusarov, D. V. Dudka, and A. V. Mityukov, "Characterization and Rheological Properties of Ultra-High Molecular Weight Polyethylenes," *Polymers* 16 (2024): 3501.

7. I. Kállai, "The Effect of Technological Parameters on the Quality of UHMWPE Products," *Materials Science Forum* 752 (2013): 233–240.

8. V. Sharma, S. Chowdhury, N. Keshavan, and B. Basu, "Six Decades of UHMWPE in Reconstructive Surgery," *International Materials Reviews* 68 (2023): 46–81.

9. P. Smith and P. J. Lemstra, "Ultra-High-Strength Polyethylene Filaments by Solution Spinning/Drawing," *Journal of Materials Science* 15 (1980): 505–514.

10. R. Schaller, K. Feldman, P. Smith, and T. A. Tervoort, "High-Performance Polyethylene Fibers "Al Dente": Improved Gel-Spinning

of Ultrahigh Molecular Weight Polyethylene Using Vegetable Oils," *Macromolecules* 48 (2015): 8877–8884.

11. A. Gebhardt, *Additive Fertigungsverfahren—Additive Manufacturing und 3D-Drucken für Prototyping—Tooling—Produktion* (Carl Hanser Verlag GmbH & Co. KG, 2016).

12. I. Gibson, D. Rosen, and B. Stucker, *Additive Manufacturing Technologies* (Springer, 2015).

13. J. J. Beaman, D. L. Bourell, C. C. Seepersad, and D. Kovar, "Additive Manufacturing Review: Early Past to Current Practice," *Journal of Manufacturing Science and Engineering* 142 (2020): 110812.

14. K. Kanishka and B. Acherjee, "Revolutionizing Manufacturing: a Comprehensive Overview of Additive Manufacturing Processes, Materials, Developments, and Challenges," *Journal of Manufacturing Processes* 107 (2023): 574–619.

15. M. Schmid, *Laser Sintering with Plastics* (Hanser, 2018).

16. DIN EN ISO ASTM 52900:2022-03, Additive Manufacturing—General Principles—Fundamentals and Vocabulary 2022.

17. D. Bourell, J. P. Kruth, M. Leu, et al., "Materials for Additive Manufacturing," *CIRP Annals* 66 (2017): 659–681.

18. T. Grimm, N. Hantke, A. Iusupova, and J. T. Sehrt, "Surface Analysis in Additive Manufacturing: a Systematic Literature Review Regarding Powder Bed Fusion Processes," *Surface Topography: Metrology and Properties* 13 (2025): 13002.

19. Y. Song, Y. Ghafari, A. Asefnejad, and D. Toghraie, "An Overview of Selective Laser Sintering 3D Printing Technology for Biomedical and Sports Device Applications: Processes, Materials, and Applications," *Optics & Laser Technology* 171 (2024): 110459.

20. R. G. Kleijnen, (Doctoral Thesis, ETH Zurich, Zurich, Switzerland 2022).

21. R. D. Goodridge, C. J. Tuck, and R. J. M. Hague, "Laser Sintering of Polyamides and Other Polymers," *Progress in Materials Science* 57 (2012): 229–267.

22. S. C. Ligon, R. Liska, J. Stampfl, M. Gurr, and R. Mülhaupt, "Polymers for 3D Printing and Customized Additive Manufacturing," *Chemical Reviews* 117 (2017): 10212–10290.

23. Y. L. Wencke, (Doctoral Thesis, Universität Hamburg, Germany 2022).

24. R. D. Goodridge, R. J. M. Hague, and C. J. Tuck, "An Empirical Study into Laser Sintering of Ultra-High Molecular Weight Polyethylene (UHMWPE)," *Journal of Materials Processing Technology* 210 (2010): 72–80.

25. Y. Khalil, N. Hopkinson, A. Kowalski, and J. P. A. Fairclough, "Characterisation of UHMWPE Polymer Powder for Laser Sintering," *Materials* 12 (2019): 3496.

26. F. Christakopoulos, P. M. H. van Heugten, and T. A. Tervoort, "Additive Manufacturing of Polyolefins," *Polymers* 14 (2022): 5147.

27. J. S. Bryant, M. J. Bortner, and C. B. Williams, "Powder Bed Fusion Additive Manufacturing of Ultra-High Molecular Weight Polyethylene Using a Novel Laser Scanning Strategy," *Additive Manufacturing* 79 (2024): 103885.

28. M. Schmid, A. Amado, and K. Wegener, "Materials Perspective of Polymers for Additive Manufacturing with Selective Laser Sintering," *Journal of Materials Research* 29 (2014): 1824–1832.

29. T. Hupfeld, A. Wegner, M. Blanke, et al., "Plasmonic Seasoning: Giving Color to Desktop Laser 3D Printed Polymers by Highly Dispersed Nanoparticles," *Advanced Optical Materials* 8 (2020): 2000473.

30. A. W. Powell, A. Stavrinadis, I. De Miguel, G. Konstantatos, and R. Quidant, "White and Brightly Colored 3D Printing Based on Resonant Photothermal Sensitizers," *Nano Letters* 18 (2018): 6660–6664.

31. J. C. Hernandez-Castaneda, B. K. Lok, and H. Zheng, "Laser Sintering of Cu Nanoparticles on PET Polymer Substrate for Printed Electronics at Different Wavelengths and Process Conditions," *Frontiers of Mechanical Engineering* 15 (2020): 303–318.

32. L. Lanzl, K. Wudy, S. Greiner, and D. Drummer, "Selective Laser Sintering of Copper Filled Polyamide 12: Characterization of Powder Properties and Process Behavior," *Polymer Composites* 40 (2019): 1801–1809.

33. D. Meng, Y. Guo, J. Li, and S. Guo, "Laser Sintering of Polyether Sulfone/Carbon Black Composite Powders Using near-Infrared Laser," *Journal of Thermoplastic Composite Materials* 36 (2023): 4707–4726.

34. M. U. Azam, I. Belyamani, A. Schiffer, S. Kumar, and K. Askar, "Progress in Selective Laser Sintering Ofmultifunctional Polymer Composites for Strain-and Self-Sensing Applications," *Journal of Materials Research and Technology* 30 (2024): 9625–9646.

35. J. D. Kechagias, N. Vidakis, K. Ninikas, M. Petousis, and N. M. Vaxevanidis, "Hybrid 3D Printing of Multifunctional Polylactic Acid/Carbon Black Nanocomposites Made with Material Extrusion and Post-Processed with CO2 Laser Cutting," *The International Journal of Advanced Manufacturing Technology* 124 (2023): 1843–1861.

36. R. Poprawe, C. Häfner, and R. Wester, *Tailored Light 2: Laser Applications* (Springer, 2024).

37. B. Acherjee, A. S. Kuar, S. Mitra, and D. Misra, "Effect of Carbon Black on Temperature Field and Weld Profile during Laser Transmission Welding of Polymers: a FEM Study," *Optics & Laser Technology* 44 (2012): 514–521.

38. Homepage Celanese, GUR 4118, https://materials.celanese.com/gb/products/datasheet/SI/GUR%C2%AE%204118 (accessed: February, 2025).

39. DIN EN ISO 60:2023-12, Plastics - Determination of Apparent Density of Material that can be poured from a specified Funnel 2023.

40. DIN EN ISO 11357-4:2021-05, Plastics - Differential Scanning Calorimetry (DSC) - Part 4: Determination of Specific Heat Capacity 2021.

41. DIN EN ISO 527-1:2019-12, Plastics - Determination of Tensile Properties - Part 1: General Principles 2019.

42. L. Benedetti, B. Brulé, N. Decraemer, K. E. Evans, and O. Ghita, "Evaluation of Particle Coalescence and Its Implications in Laser Sintering," *Powder Technology* 342 (2019): 917–928.

43. Homepage Sinterit, Lisa SLS 3D Printer, https://sinterit.com/3dprinters/lisa/ (accessed: February, 2025).

44. D. Drummer, D. Rietzel, and F. Kühnlein, "Development of a Characterization Approach for the Sintering Behavior of New Thermoplastics for Selective Laser Sintering," *Physics Procedia* 5 (2010): 533–542.

45. M. Schmid, A. Amado, and K. Wegener, *AIP Conf. Proc.* 1664 (2015): 160009.

46. A. Sommereyns, T. Hupfeld, B. Gökce, S. Barcikowski, and M. Schmidt, "Evaluation of Essential Powder Properties through Complementary Particle Size Analysis Methods for Laser Powder Bed Fusion of Polymers," *Procedia CIRP* 94 (2020): 116–121.

47. S. Yang and J. R. G. Evans, "Metering and Dispensing of Powder; the Quest for New Solid Freeforming Techniques," *Powder Technology* 178 (2007): 56–72.

48. S. E. Brika, M. Letenneur, C. A. Dion, and V. Brailovski, "Influence of Particle Morphology and Size Distribution on the Powder Flowability and Laser Powder Bed Fusion Manufacturability of Ti-6Al-4 V Alloy," *Additive Manufacturing* 31 (2020): 100929.

49. X. Hao, C. Xian, H. Wang, and L. Shen, "Preparation of Ultra-High Molecular Weight Polyethylene (UHMWPE) fiber Copper(II) Ions Adsorbent by Radiation Grafting," *Journal of Radioanalytical and Nuclear Chemistry* 331 (2022): 5569–5577.

50. J. V. Gulmine, P. R. Janissek, H. M. Heise, and L. Akcelrud, “Polyethylene Characterization by FTIR,” *Polymer Testing* 21 (2002): 557–563.

51. M. Bredács, C. Barretta, L. F. Castillon, et al., “Prediction of Polyethylene Density from FTIR and Raman Spectroscopy Using Multivariate Data Analysis,” *Polymer Testing* 104 (2021): 107406.

52. D. Han, Z. Meng, D. Wu, C. Zhang, and H. Zhu, “Thermal Properties of Carbon Black Aqueous Nanofluids for Solar Absorption,” *Nanoscale Research Letters* 6 (2011): 457.

53. F. Lupone, E. Padovano, F. Casamento, and C. Badini, “Process Phenomena and Material Properties in Selective Laser Sintering of Polymers: a Review,” *Materials* 15 (2021).

54. P. Chen, M. Tang, W. Zhu, et al., “Systematical Mechanism of Polyamide-12 Aging and Its Micro-Structural Evolution during Laser Sintering,” *Polymer Testing* 67 (2018): 370–379.

55. V. M. Lobe and J. L. White, “An Experimental Study of the Influence of Carbon Black on the Rheological Properties of a Polystyrene Melt,” *Polymer Engineering & Science* 19 (1979): 617–624.

56. J.-F. Zhang and X.-S. Yi, “Dynamic Rheological Behavior of High-Density Polyethylene Filled with Carbon Black,” *Journal of Applied Polymer Science* 86 (2002): 3527–3531.

57. B. Haworth, N. Hopkinson, D. Hitt, and X. Zhong, “Shear Viscosity Measurements on Polyamide-12 Polymers for Laser Sintering,” *Rapid Prototyping Journal* 19 (2013): 28–36.

58. A. Almabrouk Mousa, “Experimental Investigations of Curling Phenomenon in Selective Laser Sintering Process,” *Rapid Prototyping Journal* 22 (2016): 405–415.

59. A. Hashim, *Smart Nanoparticles Technology* (InTech, 2012).

60. Homepage GEHR Plastics PE-UHMW Polyethylene, Ultra High Molecular Weight, https://www.matweb.com/search/datasheet_print.aspx?matguid=22492cabc9c3487493a3dd214fc4a3dd (accessed: February, 2025).

61. J.-P. Song, K.-Y. Tian, L.-X. Ma, W. Li, and S.-C. Yao, “The Effect of Carbon Black Morphology to the Thermal Conductivity of Natural Rubber Composites,” *International Journal of Heat and Mass Transfer* 137 (2019): 184–191.

62. J. Jhabvala, E. Boillat, and R. Glardon, “Study of the Inter-Particle Necks in Selective Laser Sintering,” *Rapid Prototyping Journal* 19 (2013): 111–117.

Supporting Information

Additional supporting information can be found online in the Supporting Information section.

Supporting file: mame70053-sup-0001-SuppMat.docx